Isotopic Signatures of Carbon in the 'Los Pobres' Graphite Mine, Ronda, Spain

Anna Neubeck[1]*, Curt Broman[1], Magnus Ivarsson[2,3], Nils G. Holm[1], Martin Whitehouse[2], Sara Nilsson[4], Wolf Geppert[4] and Fernando Gervilla[5]

[1]Department of Palaeobiology, Uppsala University, Uppsala 752 36, Sweden; [2]Department of Palaeobiology, Swedish Museum of Natural History, Stockholm 114 18, Sweden; [3]Department of Biology, University of Southern Denmark, Odense 5230, Denmark; [4]Department of Physics, Stockholm University, Stockholm 106 91, Sweden; [5]Department of Mineralogy and Petrology, University of Granada, Granada 18002, Spain

*Corresponding author. Telephone: +46 (0)18 475 25 62. Fax: +46 (0)18 471 20 00. E-mail: anna.neubeck@geo.uu.se

ABSTRACT

Graphite formation temperatures in the 'Los Pobres' mine within the Ronda peridotite, Spain, previously reported to be between 770 and 820 °C, have been reinterpreted based on new temperature measurements using Raman spectroscopy. Additional *in situ* and bulk stable carbon isotopic measurements and fluid inclusion studies contributed to improved understanding of parts of the graphite formation process. Raman spectroscopy revealed that the formation of the 'Los Pobres' graphite extends to temperatures as low as 500 °C, indicating a broader temperature range than previously reported. Stable carbon isotopes and temperature estimates suggest two different crystallization events, followed by a late hydrothermal alteration of the host rock. The first event occurred at temperatures higher than ~600°C, in which crystalline graphite was formed with a mixed ^{13}C composition as a result of the mixing of two different carbon-bearing sources. The second graphite formation event took place below ~600°C, within the same system, but with lower purity and crystallinity of the graphite. In the third event, the temperature decreased to less than 550 °C, and hydrothermal fluids altered the host rock, precipitating silica and iron oxides in veins penetrating both the host rock and the deposited graphite.

Key words: Ronda peridotite; graphite formation temperature; Raman spectroscopy; carbon isotopes; fluid inclusions

INTRODUCTION

Carbonaceous matter (CM) subjected to burial and metamorphism undergoes maturation to ultimately become well-crystallized graphite. Structurally disordered carbonaceous material becomes increasingly ordered with rising temperature (T) and pressure (P). Furthermore, maturation of CM is considered to be an irreversible process, which makes T measurements of the material a reliable indicator of the peak T in its thermal history. The maturation and graphitization process of carbonaceous matter, therefore, allows for the use of carbon disorganization as a metamorphic thermometer. In a previous study of the 'Los Pobres' graphite (Luque et al., 1992), the graphite c_0 parameter obtained by X-ray diffraction (XRD) allowed estimation that the formation temperature was 770–820°C. The c_0 parameter is an indicator of maximum formation T, but because XRD requires sample disaggregation, sample preparation may alter the CM structure. Therefore, using Raman spectroscopy to characterize CM is advantageous (Beyssac et al., 2002a; Huang et al., 2010). The benefit of using Raman spectroscopy is the capability of *in situ* analyses of individual graphite grains in either polished thin sections or mineral fragments without further preparation or destruction of the sample. When using an Ar$^+$ laser, Raman characterization of CM is mainly within the spectroscopic strong first-order bands with wavenumbers between 1000 and 1800 cm^{-1} (Beyssac et al., 2002a, 2002b; Pimenta et al., 2007;

Huang *et al.*, 2010). The centre position of these Raman bands is dependent on the excitation wavelength: when using an Ar^+ laser at $\lambda = 514$ nm, the graphite band (G band) occurs between 1575 and 1590 cm^{-1}. In poorly ordered graphite or kerogens, two defect bands can be observed, D1 at approximately 1350–1360 cm^{-1} and D2 at approximately 1620 cm^{-1} (Beyssac *et al.*, 2002*a*, 2002*b*; Pimenta *et al.*, 2007; Huang *et al.*, 2010). When estimating the peak T from the degree of structural order based on the Raman bands, the area ratio AR = [D1/(G + D1 + D2)] and the correlation $T(°C) = -445AR + 641$ are used for calculations (Beyssac *et al.*, 2002*a*). The graphite geothermometer is applicable in the range of 330–650°C, and the maximum error of the T calculations is estimated at ± 50 °C. Bulk and *in situ* stable carbon isotopic analysis has been performed on the graphite material in the mineralization, as well as in veins, to track the carbon precipitation pathways and sources.

MATERIALS AND METHODS

Geological setting

The Ronda Peridotite (RP) in the Serranía de Ronda in southern Spain is mainly (90–95%) composed of partly serpentinized peridotites (<30% serpentinization), and it is the world's largest exposed massif of orogenic lherzolites. It consists of three major ultramafic outcrops, the Ronda massif, ~300 km², the Ojén massif, ~70 km², and the Carratraca massif, ~60 km², which are now interpreted as portions of a 1·3 Ga (Reisberg & Lorand, 1995; van der Wal & Vissers, 1996; Garrido & Bodinier, 1999; Lenoir, 2001; Vauchez & Garrido, 2001; Gutierrez-Narbona *et al.*, 2003) subcontinental lithospheric mantle affected by thermal alteration and chemical erosion (van der Wal & Bodinier, 1996; van der Wal & Vissers, 1996; Garrido & Bodinier, 1999; Lenoir, 2001; Vauchez & Garrido, 2001; Gutierrez-Narbona *et al.*, 2003).

These massifs show similar tectono-metamorphic zoning made (from top to bottom) of a spinel tectonite (including garnet–spinel mylonites) domain, a granular peridotite domain and a plagioclase tectonite domain (van der Wal & Bodinier, 1996; Garrido & Bodinier, 1999; Lenoir, 2001; Esteban *et al.*, 2005). The upper spinel tectonite domain represents what remains of an ancient Proterozoic garnet–spinel peridotite assemblage (Garrido *et al.*, 2011) and is separated from the underlying granular domain by a recrystallization front according to Lenoir (2001) and Vauchez & Garrido (2001). These researchers proposed that the granular peridotite domain developed at the expense of the pre-existing spinel tectonites by partial melting associated with the upward migration of melt flow and melt accumulation below the recrystallization front. The plagioclase tectonite domain developed later during the crustal emplacement of the peridotite massifs by shearing the granular peridotites. Nevertheless, Esteban *et al.* (2005) proposed a slightly different origin of the Carratraca massif based on the ascent of a young, hot diapiric plagioclase peridotitic asthenosphere, which partially melted the overlying old, cool continental lithosphere rich in organic carbon.

The RP also hosts unusual deposits composed of chromite with Ni arsenides (Cr–Ni ores) and Fe–Ni–Cu sulphides with graphite (S–G ores), which originated by the fractionation of a complex immiscible As–S–Fe–Ni-rich liquid segregated from a mafic magma. This was derived from immiscible magmas formed from the development of the granular peridotite, which accumulated below the recrystallization front (Gervilla & Leblanc, 1990; Gervilla *et al.*, 2002). Small volumes of the magma migrated above the recrystallization front, coalesced and fractionated, forming small mineralized sulphide–graphite veins. The 'Los Pobres' mine is a graphite vein deposit located in the Carratraca massif within the spinel tectonite domain (Luque *et al.*, 1992; Crespo *et al.*, 2006). It is hosted by strongly serpentinized spinel lherzolites. This mine forms part of the Los Jarales mining district, which also includes important Cr–Ni-type mineralizations (Gervilla & Leblanc, 1990). Different mechanisms have been proposed for the formation of the 'Los Pobres' graphite veins. Gervilla & Leblanc (1990) considered the graphite veins to be the result of hydrothermal alteration of primary S–G-type mineralization whose parent melt could incorporate carbon via melt–rock reactions of graphite-bearing pyroxenites with infiltrating asthenospheric melts (Crespo *et al.*, 2006; Huang *et al.*, 2010). Luque *et al.* (1992) also proposed that the 'Los Pobres' graphite vein and the Mina Marbella deposit originated from magmatic processes (separation of immiscible magmas) but involving crustal incorporation of biogenic carbon during emplacement. These researchers argued that serpentinization is an unlikely explanation because of the high estimated temperatures of the vein assemblages, as well as the indications of an oxidizing environment owing to the presence of magnetite. This study aims to reinvestigate the formation of the graphite and evaluate the influences of serpentinization on the paragenesis of the graphite mineralization using Raman spectroscopy and stable carbon isotopes.

Samples

All samples were collected in the 'Los Pobres' mine within and in close proximity to a large graphite occurrence (Fig. 1, a–c). Doubly polished thin sections of 200 µm thickness (Ivarsson, 2006) were prepared from the samples (Fig. 1, d). The samples included (1) hand-specimens of graphite, serpentine, fracture fillings (hereafter called veins) and contact between graphite and serpentine, and (2) doubly polished thin sections of the graphite and the serpentine (sampled profile above and below the graphite).

Methods

Mineralogical analyses and determination of the structural order of graphite were carried out by Raman spectroscopy on both hand-specimens and polished
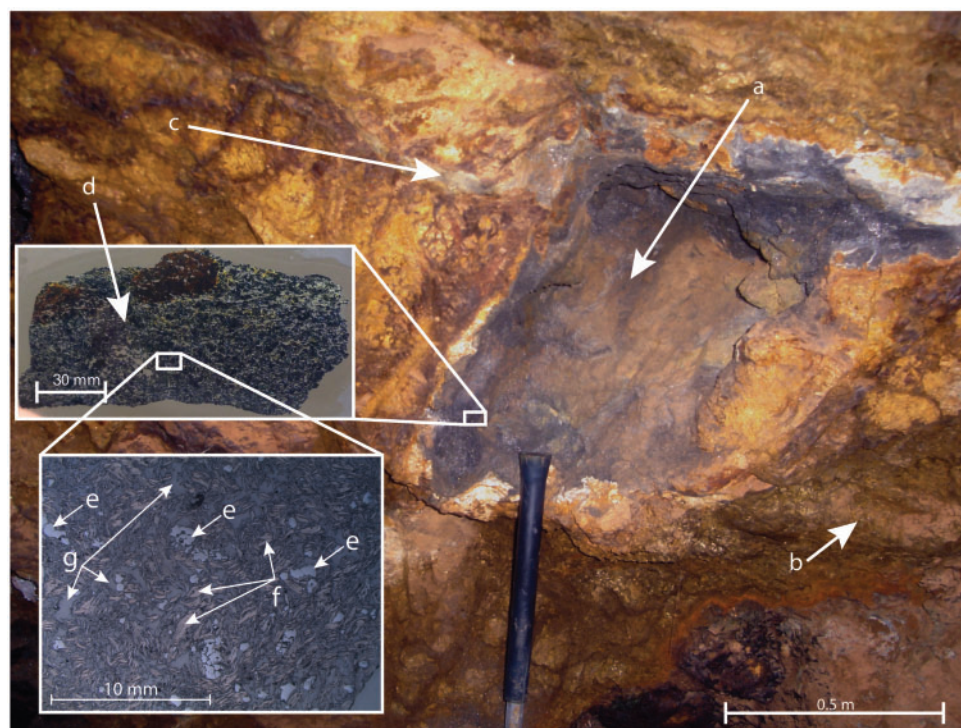
Fig. 1. Graphite mineralization in serpentine. Strongly serpentinized lherzolite host rock demonstrating (a) the graphite mineralization, (b) the serpentinized host rock, (c) a graphite vein crosscutting the graphite, (d) the heterogeneity of the graphite mineralization in a thin section, (e) irregularly shaped grains within the graphite (chromite grains), (f) graphitic flaky grains and (g) the graphite matrix. The last inset figure is an optical microscope image using reflected light.

sections in two different measuring cycles. The first round of measurements was made in Aberdeen on a Renishaw inVia Reflex Spectrometer, with Renishaw WiRE 2.0 software used for data processing. All the spectra were measured using ×50 magnification to focus the Ar$^+$ laser beam and with three accumulations of 6 s duration at 50 % power (total laser power approximately 10 mW).

The second round of Raman analysis (including fluid inclusions) was made at the Department of Geological Sciences, Stockholm University, using a Horiba instrument LabRAM HR 800 laser Raman confocal spectrometer equipped with a multichannel air-cooled CCD detector. An Ar-ion laser ($\lambda = 514$ nm) was used as the excitation source. The instrument was integrated with an Olympus microscope, and the laser beam was focused on a 1 μm spot with a ×100 objective. The spectral resolution was approximately 0·3 cm^{-1}. Data acquisition was performed on graphite with a low output power (1 mW) at the sample and a 1 s exposure for each measurement to avoid alteration of the graphite surface by the laser. Data acquisition of fluid inclusions and other mineral analyses was performed with 10 accumulations of 10 s each (10 × 10 s). The instrument was calibrated using a Ne lamp and the Raman line of a Si wafer (520·7 cm^{-1}). Instrument control and data acquisition were made with LabSpec 5 software.

Care was taken to avoid alteration of the CM structure by the laser (by comparing spectra at different laser powers, numbers of iterations and exposure times). All analyses on the doubly polished thin sections were made by focusing the laser beneath the surface to avoid possible effects created during the preparation procedure (Beyssac *et al.*, 2002*a*). For non-polished hand-specimens, this was not a problem. Significant changes in the Raman spectra owing to mechanical polishing have been reported (Beyssac *et al.*, 2003; Nasdala *et al.*, 2004) and to avoid any misinterpretations Raman analyses were also performed on unpolished grains from the thin section preparation blocks, where unpolished grains could be found in small voids. Raman spectra were also collected from hand-specimens to validate the peak positions of the thin section spectra. Although the orientation of the graphite crystals may have a considerable impact on Raman spectra (Katagiri *et al.*, 1988; Wang *et al.*, 1989; Compagnini *et al.*, 1997), the AR for the *T* calculation does not change significantly between 340 and 650 °C (Kouketsu *et al.*, 2014).

Fluid inclusion microthermometry was performed on a Linkam THM600 heating and freezing stage mounted on a Nikon microscope and utilizing a long working-distance ×40 objective.

Environmental scanning electron microscopy (ESEM) was used to estimate the elemental composition and to investigate the mineralogy of the samples. All measurements were performed at the Department of Geological Sciences, Stockholm University, on a Fei Quanta 650 FEG equipped with a backscatter and a
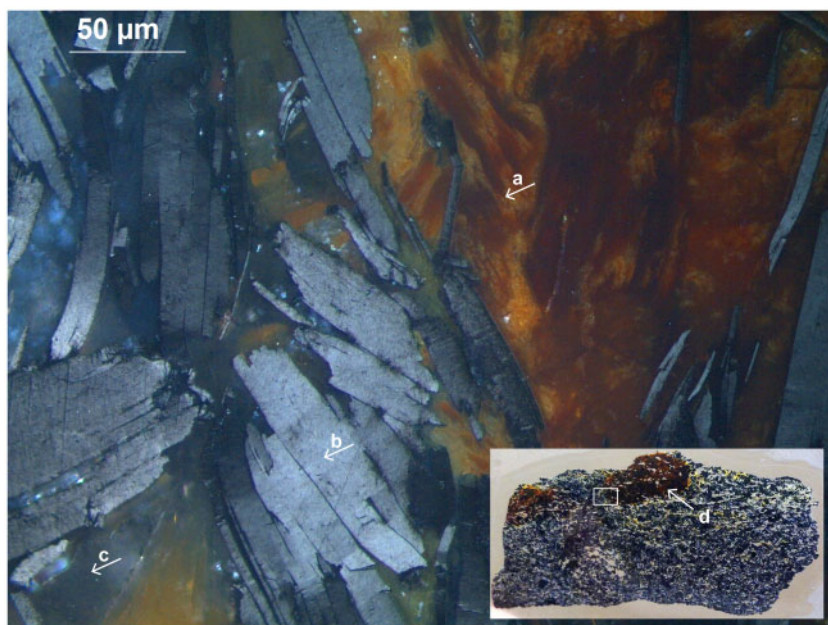
Fig. 2. Graphite thin section. A microscopy image (transmitted light) of the different graphite phases in which (a) is the Fe-rich matrix, (b) is the flaky graphite, (c) is the Si-rich matrix and (d) indicates the Fe-rich areas. The white square within the inset shows the location of the magnified larger area.

secondary electron detector used for all measurements. Both high and low vacuum were used for the analyses. Data processing software was Oxford AZtec and Oxford Inca using Oxford Tru-Q technology.

Bulk carbon isotopes were measured at the stable isotope laboratory (SIL), Department of Geological Sciences, Stockholm University, on a Carlo Erba elemental analyzer NC 2500 coupled to a Delta V Advantage mass spectrometer from Thermo Scientific. δ^{13}C values are expressed in per mil differences with respect to the V-PDB (Peedee Belemnite) standard. Twelve measurements per sample were made to ensure statistically reliable results and to identify a potentially large spread among the measurements. *In situ* stable carbon isotopes were measured by secondary ion mass spectrometry (SIMS) using a Cameca IMS 1280 NORDSIM system at the Swedish Museum of Natural History (Stockholm, Sweden). Polished thin sections were mounted on a stainless steel sample holder with an S0161 cc carbon isotope standard.

RESULTS

Mineralogy, morphology and elemental composition

The graphite was hosted by strongly serpentinized rocks. Chrysotile was the main secondary serpentine mineral in the Ronda massif, with minor amounts of lizardite (Esteban, 2011). Late brown–red veins crosscut the serpentinized rock and the graphite mineralization (Fig. 1, a–c). Raman spectroscopy showed that these veins are mainly composed of secondary amorphous silica (formed by serpentinization of the host rock), amorphous iron oxyhydroxide and crystalline goethite. The samples

were graphite-bearing and consisted of a fine-grained silicified serpentine with a few fractured relics of primary mineral grains composed of spinel and enstatite. The graphite matrix was dominated by a colourless to greyish variety (Fig. 1, d) with yellow–brown coloured areas. Some of the graphite grains were irregularly shaped (Fig. 1, e), some were flaky (Fig. 1, f), and others were composed of a homogeneous matrix (Fig. 1, g). Figure 2 shows the yellow–brown matrix (Fig. 2, a and d), flaky grey crystals (Fig. 2, b), and the colourless to greyish matrix (Fig. 2, c) in a thin section illuminated by transmitted light. Both types of matrix were extensively altered.

ESEM (Supplementary Fig. 1; supplementary data are available for downloading at http://www.petrology. oxfordjournals.org) and Raman measurements show that the yellow–brown matrix was Fe-rich with a hydrous $(Mg,Fe)_{2n+1}(SiO_4)_n(OH)_2$-like structure (similar to humite minerals; Frost *et al.*, 2008), whereas the colourless to greyish matrix was Si-rich and mainly consisted of amorphous silica.

The fractured spinel grains were dark reddish-brown and randomly distributed within the samples. ESEM revealed a composition of Al, Mg, Cr and Fe, which is consistent with a Cr-spinel composition with Al substitution (Supplementary Fig. 1). The Raman spectrum of the spinel was complex (Supplementary Fig. 2) and suggested a Cr spinel comparable with the general formula $(MgFe^{2+})(Al,Cr)_2O_4$ (Lenaz & Lughi, 2013). Based on the RRUFF database of Raman spectra (Downs, 2006), the bands at 306, 405, ∼650 and 754 cm^{-1} are characteristic of $(MgAl_2O_4)$ spinel, the band at 625 cm^{-1} may be assigned to magnesioferrite $(MgFe_2O_4)$, and the bands at 483, 540 and 702 cm^{-1} correspond to Fe-chromite $(FeCr_2O_4)$. Electron microprobe analyses show a similar
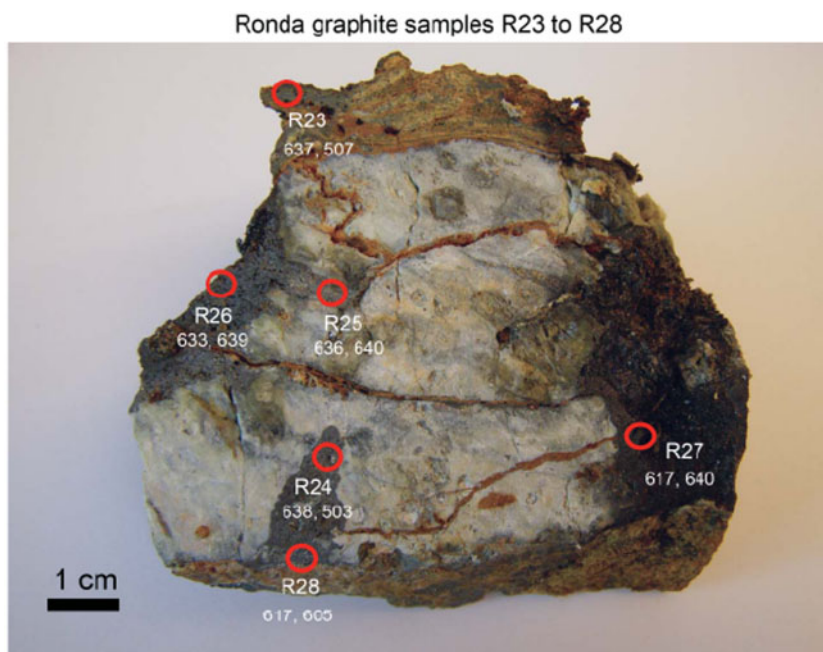
Fig. 3. Rock sample including serpentine, iron oxides and graphite. Hand-specimen of the rock surrounding the graphite deposit, with red circles showing the positions of Raman analyses. Two separate graphite grains were measured within every circle.

intermediate composition between chromite ($FeCr_2O_4$)–magnesiochromite ($MgCr_2O_4$)–spinel ($MgAl_2O_4$)–hercynite ($FeAl_2O_4$) (Supplementary Table 1). Raman analyses were performed at 36 randomly distributed spots on graphite samples with fresh and non-weathered surfaces. The spot analyses R1–R10 were recorded on graphitic matrix, R11–R20 on graphite grains, R21, R29 and R30 on graphite nodule-like accumulations and clumps, and R22 and R23–R28 (Fig. 3) on mixtures of massive graphite accumulations and veins.

Thus, the AR is zero and suggests a corresponding temperature above the upper working limit >640°C for the graphite geothermometer (Beyssac *et al.*, 2002*a*, 2002*b*). Graphite in a vein sample had the least ordered structure and was characterized by a G band at $1580\,cm^{-1}$, together with a D1 band near $1360\,cm^{-1}$ and a D2 band at $1620\,cm^{-1}$ (Fig. 4b). The AR is 0·316, which indicates a peak *T* of 500°C. The whole range of Raman data for the graphite samples indicates peak *T* between 500° and ≥640°C (Table 1). The lower temperatures were mainly obtained in vein graphite, but the heterogeneity of structural order and estimated graphite-forming *T* amongst adjacent graphite grains were generally found at a microscopic scale depending on differences in their morphologies. This can be illustrated by the example in Supplementary Fig. 3 at a higher magnification, in which well-ordered flaky grains with a *T* of 637°C are surrounded by granular aggregates of cryptocrystalline graphite with a *T* of 503°C.

Fluid inclusions

Most of the primary minerals in the serpentinized rock have disappeared, except spinel and enstatite. Spinel is
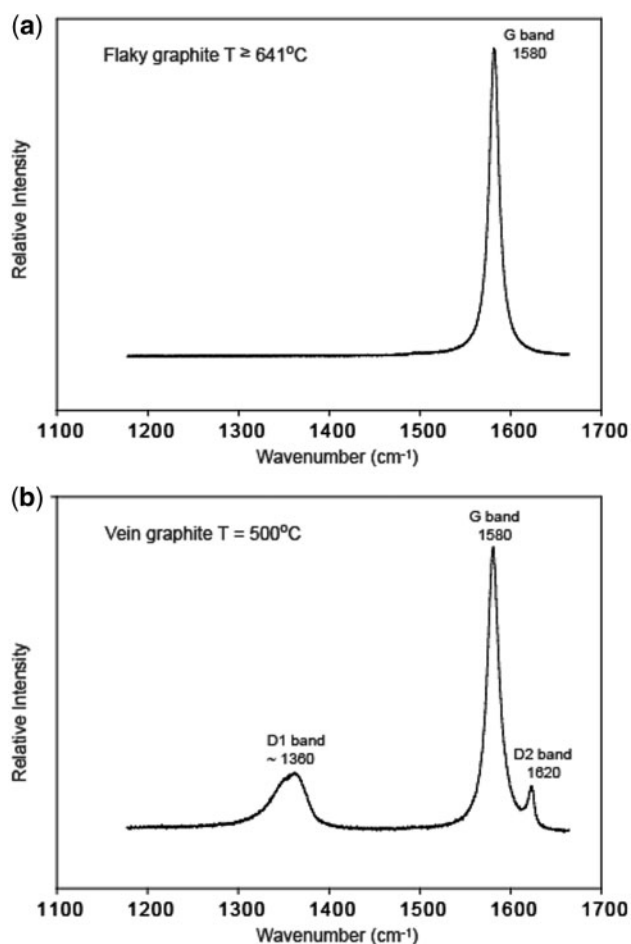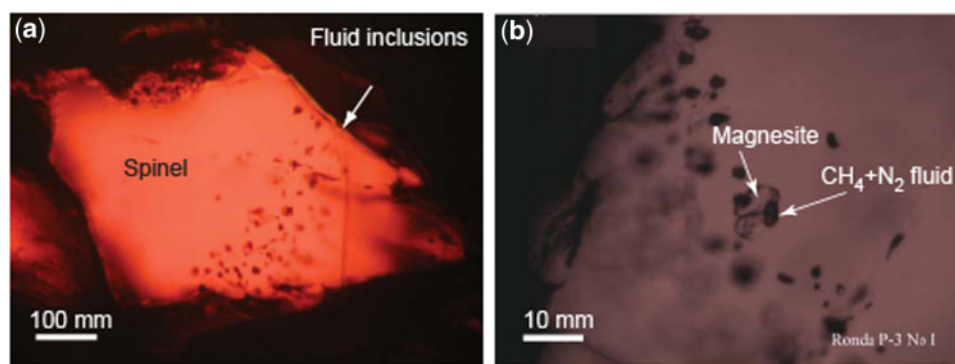

Fig. 4. Raman spectra flaky graphite (a) and vein graphite (b). The Raman spectra indicate a higher structural order and peak *T* for the nodule (>650°C) than for the vein (500°C).

Table 1: Graphite samples measured using Raman spectrometry and with calculated temperatures from formulae, according to Beyssac et al. (2002a)

Sample no.	Type of graphite	Graphite band $\sim 1360\,cm^{-1}$ D1	Graphite band $1580\,cm^{-1}$ (including $1620\,cm^{-1}$), G + D2	Area ratio D1/(G + D1 + D2)	Temperature (°C) ($T = -445 \times$ area ratio $+ 641$)
R1	Matrix	6104	97912	0·062	613
R2	Matrix	12944	119016	0·109	592
R3	Matrix	5521	85841	0·064	612
R4	Matrix	32442	151116	0·215	545
R5	Matrix	—	74697	0	≥641
R6	Matrix	14996	124578	0·120	587
R7	Matrix	2969	89462	0·033	626
R8	Matrix	6029	92707	0·065	612
R9	Matrix	4122	82028	0·050	618
R10	Matrix	—	77474	0	≥641
R11	Inclusion	5212	81590	0·064	612
R12	Inclusion	7819	31727	0·246	531
R13	Inclusion	13312	144263	0·092	600
R14	Inclusion	29540	157471	0·188	557
R15	Inclusion	48096	167268	0·287	513
R16	Inclusion	9219	83429	0·110	592
R17	Inclusion	—	82290	0	≥641
R18	Inclusion	1112	73448	0·015	634
R19	Inclusion	11449	90148	0·127	584
R20	Inclusion	5619	87178	0·064	612
R21	Nodule	—	48272	0	≥641
R22	Vein	8170	25840	0·316	500
R23-a	Massive	491	55938	0·009	637
R23-b	Vein	47403	109427	0·302	507
R24-a	Massive	435	76561	0·006	638
R24-b	Vein	13014	28947	0·310	503
R25-a	Massive	816	69952	0·011	636
R25-b	Massive	79	37130	0·002	640
R26-a	Massive	1359	75261	0·018	633
R26-b	Massive	282	74920	0·004	639
R27-a	Massive	2411	42696	0·053	617
R27-b	Massive	47	29302	0·002	640
R28-a	Massive	2807	49501	0·054	617
R28-b	Massive	3519	40434	0·080	605
R29	Nodule	—	20487	0	≥641
R30	Nodule	—	48689	0	≥641

Fig. 5. Optical microscopy images showing fluid inclusions. (a) Trail of secondary fluid inclusions in a healed microfracture in Cr-spinel; (b) typical dark fluid inclusions in the trail and fluid inclusion composition.

relatively highly resistant to alteration compared with other minerals such as olivine and pyroxene. Any existing pre-serpentinization fluid inclusions in the rock had been destroyed. A few fluid inclusions were found in a relic dark red and clear Cr-spinel (Fig. 5a). All inclusions were secondary and considered to have been trapped during the healing of a microfracture in the spinel when the surrounding rock was serpentinized. The fluid inclusions were less than 10 μm in diameter and difficult to observe, partly because of the dark host spinel but also owing to their shape. The inclusions had an irregular round shape with a dark fluid-filled cavity and a lumpy light solid phase surrounded by a circular thin film of fluid (Fig. 5b). Despite several attempts to distinguish phase transitions in the central cavities with microthermometry, no change could be noticed.
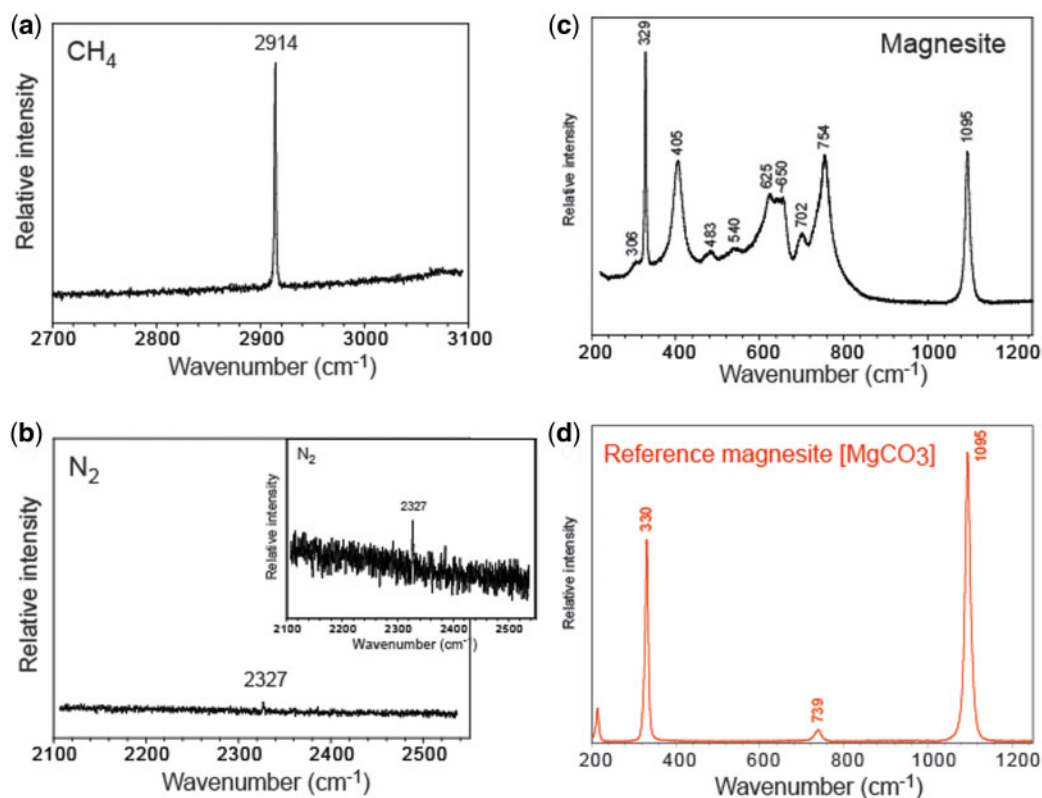
Fig. 6. Raman spectra obtained from fluid inclusions in spinel. Raman spectrum of (a) CH_4 and (b) N_2. The Raman spectrum of the lumpy light solid phase identified as (c) magnesite ($MgCO_3$) compared with (d) a magnesite reference spectrum RRUFF ID: R050443 from the RRUFFTM project (Downs 2006). The other Raman bands are from the host Cr-spinel.

The fluid inclusions were analysed using Raman microspectroscopy to identify the fluid and solid phases. The acquired spectra (Fig. 6a) show that the dark fluid-filled cavities consisted of CH_4, as revealed by the band at 2914 cm^{-1}, and N_2, as shown by the band at 2327 cm^{-1} (Fig. 6b). Because the signal from N_2 was weak compared with that from CH_4, the scale of the 'relative intensity' axis was adjusted in the inset spectrum to make the N_2 band more visible. Raman analysis detected no additional gas species. From the Raman data, a semiquantitative fluid composition of approximately 80–85 mol% CH_4 and 15–20 mol% N_2 is indicated according to equation (1) of Frezzotti *et al.* (2012). The lumpy light solid phase contained within the fluid inclusions was revealed by Raman spectroscopy to be magnesite ($MgCO_3$) with characteristic bands at 329 and 1095 cm^{-1} (Fig. 6c). The band at 739 cm^{-1} observed in the reference spectrum (Fig. 6d) is overlapped by the signal from the host mineral Cr-spinel.

Carbon isotopes

Graphite was mechanically separated from unweathered surfaces at different points of the nodule-like accumulations and the vein-type occurrence. Twelve graphite samples were collected from the nodule-like graphite aggregate close to R27 (Fig. 3), 14 were collected for the vein analyses close to R23 (Fig. 3) and 11 host-rock serpentine samples were measured. Bulk

carbon isotopic ratios ($\delta^{13}C$) of the analysed graphite fall within a narrow range in each sample type, from –18·43 to –18·66‰ (V-PDB) with an average ($n = 10$) value of –18·52 ± 0·07‰ for the nodule-like graphite aggregates (Fig. 1) and from –30·36 to –33·90‰ (V-PDB) with an average ($n = 10$) value of –32·35 ± 1·17‰ for the graphite veins (Table 2).

The isotopic composition of the graphite nodule was considerably heavier than that of the surrounding serpentine material (Table 2, Sample P-5 to P6, excluding P0, which is graphite) the average of which was –23·83 ± 1·15‰ ($n = 11$). Carbon isotopes measured *in situ* revealed a range of isotope values clustering around an average ($n = 69$, Table 2) of –15·92 ± 0·28‰; a few (four out of 69) lower values averaging –22·42 ± 0·41‰ (Table 2) were discarded. No values were lighter than –24·59‰. All light ($< -20‰$) values were measured from cavities in the sample, whereas all other values originated from the graphite crystals. A difference was observed in one of the sampling profiles that passed through a vein and into the graphite where the vein isotopic signatures were lighter (–18·26 ± 0·38‰) than the median value (–15·97 ± 0·57‰) but increased towards the graphite to heavier values (–14·96 ± 0·29‰). No isotope signatures could be analysed within the chromite grains or the silica-rich veins owing to a lack of measurable carbon content. The $\delta^{13}C$ values of the matrix graphite could not be measured by *in situ* analyses

Table 2: *In situ* and bulk stable carbon isotope ratios in ‰; *in situ* vs PDB measured on 10 sampling points per sample type (graphite mineralization and vein)

Sample no.	^{12}C c.p.s. ($\times 10^9$)	^{12}C$_{samp/av.std}$	δ^{13}C vs PDB, ‰	±‰	Graphite type
B1	0·24	0·99	−15·44	0·28	flaky
B3	0·15	0·6	−16·95	0·33	flaky and matrix
B5	0·15	0·61	−21·12	0·39	cavity
B7	0·14	0·58	−15·3	0·32	flaky
B8	0·26	1·08	−16·6	0·29	flaky and matrix
B9	0·18	0·72	−15·82	0·29	flaky
B10	0·1	0·39	−18·73	0·3	flaky and matrix
B11	0·27	1·12	−16·54	0·26	flaky and matrix
C2	0·12	0·48	−18·25	0·38	flaky and matrix
C4	0·29	1·19	−15·73	0·27	flaky
C5	0·17	0·7	−16·03	0·3	flaky and matrix
C8	0·16	0·68	−15·23	0·35	flaky
C9	0·26	1·12	−15·54	0·27	flaky
C11	0·12	0·5	−17·92	0·39	flaky and matrix
C13	0·28	1·17	−16·54	0·27	flaky
C15	0·27	1·13	−16·79	0·27	flaky
C16	0·27	1·16	−15·94	0·27	flaky
C17	0·09	0·38	−16·3	0·37	flaky and matrix
C18	0·27	1·14	−16·34	0·26	flaky
C19	0·32	1·37	−14·92	0·26	?
C21	0·23	0·98	−15·64	0·28	flaky
C22	0·24	1·05	−15·82	0·27	flaky
C25	0·28	1·22	−15·82	0·29	flaky
C26	0·28	1·23	−14·84	0·26	flaky
C40	0·19	0·8	−16·61	0·29	?
C45	0·19	0·81	−16·2	0·31	flaky (w/in vein)
C47	0·28	1·2	−15·58	0·27	flaky and matrix
C48	0·31	1·29	−15·45	0·27	flaky
C49	0·27	1·11	−14·31	0·28	flaky
C50	0·28	1·18	−15·4	0·26	flaky
C51	0·28	1·16	−15·02	0·28	flaky
C52	0·26	1·1	−16·03	0·27	flaky
C53	0·29	1·19	−14·96	0·29	flaky
C56	0·28	1·2	−15·66	0·27	flaky
C57	0·26	1·1	−15·83	0·3	flaky
C60	0·28	1·19	−15·91	0·26	flaky
C61	0·28	1·21	−16·84	0·27	flaky
C63	0·27	1·15	−16·7	0·27	flaky
C64	0·28	1·2	−17·46	0·27	flaky
C66	0·17	0·73	−16·24	0·32	flaky and matrix
C69	0·28	1·18	−15·6	0·3	flaky
C70	0·24	1·04	−15·97	0·28	flaky
C71	0·28	1·18	−16·9	0·27	flaky
CR1	0·3	1·21	−15·68	0·27	flaky
CR2	0·3	1·22	−15·7	0·26	flaky
CR3	0·3	1·21	−15·38	0·28	flaky
CR5	0·13	0·5	−16·71	0·31	flaky and matrix
CR7	0·29	1·2	−15·69	0·29	flaky
D2	0·28	1·22	−13·5	0·27	flaky
D3	0·27	1·19	−15·82	0·27	flaky
D5	0·25	1·09	−15·87	0·28	flaky
D15	0·15	0·66	−16·94	0·33	flaky
D16	0·27	1·18	−15·58	0·26	flaky
D17	0·26	1·14	−15·82	0·26	flaky
PR4	0·23	0·99	−19·67	0·27	flaky
PR5	0·26	1·11	−16·25	0·26	flaky
PR8	0·23	0·97	−17·87	0·29	cavity
PR9	0·11	0·48	−15·14	0·38	cavity
PR10	0·28	1·17	−15·55	0·28	flaky
RGR5	0·13	0·54	−18·63	0·34	flaky and matrix
RGR6	0·11	0·49	−16·99	0·35	flaky and matrix
RGR7	0·27	1·17	−16·93	0·26	flaky
RGR9	0·27	1·16	−16·27	0·27	flaky
RGR10	0·13	0·56	−18·51	0·41	flaky and matrix
UGR1	0·31	1·25	−16·83	0·28	flaky
UGR2	0·11	0·47	−22·8	0·32	flaky and matrix
UGR6	0·21	0·86	−21·87	0·36	flaky and matrix
UGR8	0·1	0·42	−21·74	0·56	flaky and matrix
UGR9	0·1	0·42	−24·59	0·44	flaky and matrix

(continued)

Table 2: Continued

Sample	Bulk sample $\delta^{13}C$		
	$\delta^{13}C_{tot}$ vs PDB (‰)	Average	SD
Graphite	−18·55	−18·52	0·07
Graphite	−18·53		
Graphite	−18·55		
Graphite	−18·48		
Graphite	−18·44		
Graphite	−18·43		
Graphite	−18·48		
Graphite	−18·56		
Graphite	−18·5		
Graphite	−18·66		
Vein	−32·83	−32·35	1·17
Vein	−32·97		
Vein	−31·59		
Vein	−33·9		
Vein	−30·78		
Vein	−33·49		
Vein	−33·18		
Vein	−31·78		
Vein	−30·36		
Vein	−32·63		

Sample	Weight (mg)	$\delta^{13}C_{tot}$ vs PDB (‰)	%C
P6 (serp)	10·43	−23·22	0·05
P5 (serp)	11·28	−25·31	0·12
P4 (serp)	9·09	−24·42	0·04
P3 (serp)	10·41	−25·52	0·15
P2 (serp)	11·08	−27·23	0·31
P1 (serp)	11·08	−24·18	0·10
P0 (graph)	5·15	−18·34	12·23
P-1 (serp)	10·82	−20·14	0·04
P-2 (serp)	10·38	−23·45	0·05
P-3 (serp)	9·98	−21·75	0·04
P-4 (serp)	10·27	−22·11	0·04
P-5 (serp)	11·57	−24·84	0·05

because the count rate was outside our user-defined limit relative to the count rate in the standards (usually set at ±30–50%). However, some *in situ* measurements overlapped a flaky crystal and matrix graphite, and these values together with the bulk analyses resulted in an average value of −17·78 ± 0·35‰, slightly lighter than the flaky graphite.

DISCUSSION

Temperature calculations for graphite formation in the 'Los Pobres' mine were estimated to range between 770 and 820 °C in an earlier study using XRD (Luque *et al.*, 1992), and its origin was proposed to be the result of magmatic processes (separation of immiscible magmas) but involving crustal incorporation of biogenic carbon during emplacement. The interpretation concluded that graphite formation through serpentinization was unlikely owing to the high estimated *T* and oxidizing conditions (evidenced by the presence of magnetite).

Our study aimed to reinvestigate the origin of the graphite using carbon isotopes and Raman spectroscopy to estimate the formation *T* and isotopic signatures of the graphite mineralization. The formation temperatures differed between flaky graphite, matrix
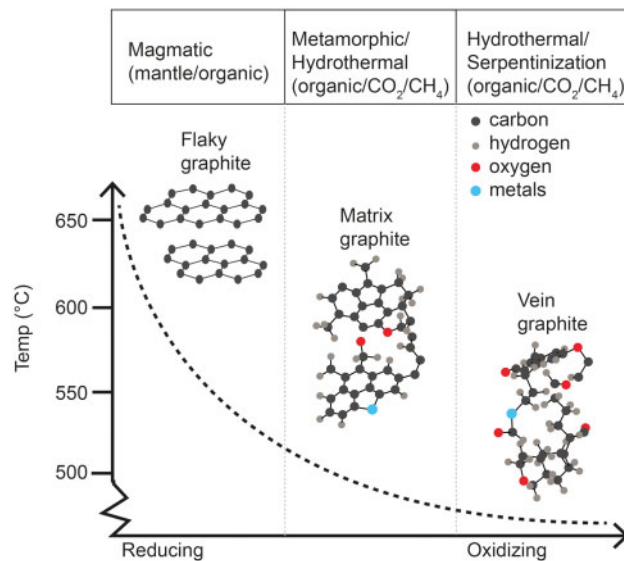

Fig. 7. Temperature decrease coupled to increased graphite disorder and oxidizing conditions.

and veins and are thought to represent three different generations of graphite formation: magmatic, metamorphic and hydrothermal (Fig. 7). According to the crystal succession in the 'Los Pobres' graphite, a first,

fluid graphite-crystallization event (mixed mantle + organic carbon) was followed by a slightly oxidized, metamorphic event (presence of magnetite and more negative carbon isotopic composition) and, finally, a serpentinization-related event, which is consistent with the isotopic signatures. Thus, we propose a more detailed model in which the 'Los Pobres' graphite developed, divided into separate generations influenced by different tectonic and geochemical processes.

Flaky graphite
The graphite in Los Pobres consists of large mineralizations of probably pure graphite, which on closer observation show distinct differences in crystallinity and elemental composition. Based on our Raman and isotope analyses, the first generation of graphite formation at 'Los Pobres' is represented by the flaky graphite. The flaky graphite crystals have a proposed magmatic origin (Luque *et al.*, 1992), which would prevent the use of geothermometry by Raman scattering (Galvez *et al.*, 2013) as the method requires carbonaceous carbon. A magmatic origin of the flaky graphite is also supported in this study by the highly ordered D1 band, which is small to non-existent relative to the sharp and well-resolved G band (Fig. 4a). The heavy $\delta^{13}C$ signature ($-15.92 \pm 0.28\%_{oo}$) indicates a mixed mantle and organic carbon signal for the flaky crystals. Our results are consistent with previous studies indicating that the first generation of graphite originated from carbon produced by the emplacement of ultramafic rocks, leading to precipitation of reduced carbon as flaky crystals of pure graphite (Figs 1, f, 2, b and 3). Thus, this is interpreted as a mix of biogenic and mantle-derived carbon (Gervilla & Leblanc, 1990; Luque *et al.*, 1992; Luque and Rodas, 1999). It has been suggested (Dickey and Obata, 1974; Luque *et al.*, 1992) that the organic matter originated from carbonaceous sedimentary rocks, the Blanca Unit, forming parts of the graphite through metamorphic evolution (Rodas *et al.*, 2000). Crustal emplacement involving lithospheric mantle and continental or sub-continental crust with subsequent metamorphism and hydrothermal alteration has been shown to result in a mixed carbon isotopic signature seldom less than $-25\%_{oo}$ (Gervilla *et al.*, 1996; Luque *et al.*, 1998; Negro *et al.*, 2006), which is consistent with our results.

Matrix and vein graphite
Geothermometry measurements of the graphitic matrix (both Si- and Fe-rich) resulted in a formation temperature range between ~545 and 630 °C, whereas temperatures <500 °C were found in the vein graphite. These temperatures are considerably lower than previously reported (Luque *et al.*, 1992) and indicate several generations (and possibly also several mechanisms) of graphite precipitation. These values are consistent with the formation temperatures of the Carratraca area in which 'Los Pobres' is situated. The temperatures of the Carratraca area are between 330 and 500 °C (Negro *et al.*, 2006) and are a result of a metamorphic evolution of peridotitic massifs of an initial magmatic event.

The bulk and *in situ* $\delta^{13}C$ values of the matrix graphite were very similar ($18.52 \pm 0.07\%_{oo}$ and $18.51 \pm 0.35\%_{oo}$, respectively) and are interpreted to be mixed signatures of flaky graphite and low-grade metamorphic graphite. The isotopic signature of the matrix is lighter than that of the flaky graphite and is the result of either an additional source of organic matter or a progressive depletion of heavy isotopes from the fluids while graphite precipitates. Low-grade metamorphic graphite is usually isotopically lighter than high-grade metamorphic graphite and would thus result in the same pattern as observed in our graphite, with flaky graphite heavier than the disordered graphite in the matrix (Luque *et al.*, 2012). However, it has also been suggested that the oxidized phase is commonly enriched in the heavier isotope (Luque *et al.*, 2012), which is contrary to what was found in this study. This is, however, true for a system in which two mineral phases precipitate concomitantly, which is probably not the case in our system where the flaky graphite crystallized prior to the matrix graphite. In a system in which graphite precipitates from organic matter, the CH_4 gas becomes depleted in ^{13}C, and the graphite enriched in ^{13}C, which is consistent with our results, in which fluid inclusions show CH_4 as the dominant gas (Fig. 5).

The vein graphite probably had a different carbon origin, with average $\delta^{13}C$ values of $-32.35 \pm 1.17\%_{oo}$, which is indicative of a large organic matter influence. The structural order of the vein graphite measured with Raman spectroscopy showed clear peaks of disordered carbon (Fig. 4). In poorly ordered carbons, a third D-band sometimes appears at 1500 cm^{-1} (Beyssac *et al.*, 2002), but this is very weak and usually not visible in natural samples. The D3 peak in our samples could neither be confirmed nor disproved as the minute peak in the spectrum at the D3 position was too small to confirm a presence.

Bulk carbon isotopes from the graphite mineralization had a considerably heavier isotopic signature ($-18.34 \pm 1.15\%_{oo}$) than serpentinized host rock ($-23.83 \pm 1.15\%_{oo}$). This is also consistent with a later hydrothermal alteration event in which organic carbon-rich fluids altered the host rock through serpentinization and imparted a lighter isotopic signal. Flaky graphite is usually the result of metamorphic processes, whereas colloform, tube or cone structures are interpreted as precipitations from carbon-bearing fluids (Luque *et al.*, 2012). This is supported by the bulk carbon isotope values, in which even larger differences between the host-rock graphite and the vein graphite were found.

Fluid inclusions
Fluid inclusions in spinel offer the possibility of revealing the conditions of graphite precipitation and interpreting the role of the trapped fluid. A system regarded

as closed leads to a depletion of graphite in the remaining fluid but a conservation of the Xo,** oxygen/(oxygen + hydrogen) ratio (Huizenga, 2010). Conservation of Xo** will result in a net reaction
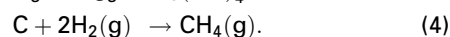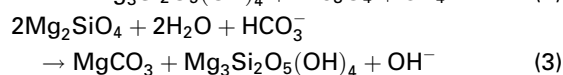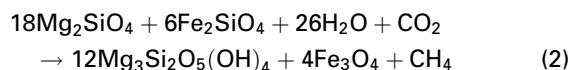
$$CH_4 + CO_2 \rightarrow 2C + 2H_2O \tag{1}$$

from which magnesite and graphite can precipitate from the CO_2-enriched fluids (from the degradation of organic matter) and from which graphite can also precipitate directly from CH_4 (reduced fluids stabilized by peridotites). This event results in the formation of aqueous fluids with the capacity to initiate a serpentinization reaction of the peridotitic host rock.

This second event resulted in a poorly crystalline, slightly oxidized graphitic matrix with a composition that is different from that of the flaky graphite crystals (Fig. 3). The flaky graphite crystals are strongly reduced but also lower in residual Fe and Si than the more oxidized graphitic matrix (Fig. 3), which incorporates insoluble oxidized minerals (i.e. arsenate and magnetite). Still, the fluids partly derive from the remelting of the Blanca Los Reales units (González-Jiménez *et al.*, 2017), forming a mix with a lighter isotopic signal. As the fluid continues to precipitate graphite, there is an increase in $f_{O_2}^{fluid}$ relative to the FMQ (fayalite–magnetite–quartz) redox buffer assemblage, which explains the slightly more oxidized graphitic matrix shown in Fig. 3. Because reaction (1) also leads to a formation of water within the system, a hydrothermal alteration will occur concomitantly or subsequently with the cooling and precipitation of the first two graphite precipitation events. The light carbon isotopic signals in the veins measured in this study could, therefore, be the consequence of the precipitation of graphite from only the fluids of the Blanca or Los Reales unit. This would explain not only the lighter isotopic signals in the veins but also the isotopic zoning that is observed in some of the previously analysed graphites (Crespo *et al.*, 2006).

The observed graphite generations in this study are interpreted to be the result of slow cooling and successive precipitation of graphite, leading to a gradually changed composition of the residual, aqueous fluid. The residual fluid will continue to cool and precipitate graphite but with changing composition and crystallinity. Water will be one of the products of the cooling, which will alter the system hydrothermally, causing the host rock to be serpentinized. The temperature range for high-T serpentinization is between ~300 and 600 °C (Evans, 2010; Majumdar *et al.*, 2016), which is consistent with former T estimates for the area (Negro *et al.*, 2006) and our Raman data showing formation temperatures of <500 °C. Oxidation [reactions (2) and (3); see below] and leaching of the original sulphur and Ni will leave a residuum of Fe oxides, As species, corroded chromites and an oxidized graphitic matrix (Fig. 2, a). Traces of the original sulphides have been found in the weathered Sulphide-Graphite (S-G) ores and were studied in detail by Crespo *et al.* (2006). Depending on

the altered primary mineral compositions, the residual matrix composition will vary accordingly, causing the different graphite matrix compositions shown in Fig. 2.

A strong indication for a hydrothermal alteration of a primary S-G-type mineralization is the presence of magnesite and methane together (Klein & McCollom, 2013; Lafay *et al.*, 2014) within the inclusions found in the chromite grains (Figs 5 and 6), as well as the inclusions that crosscut the grain and follow visible healed fractures. Serpentinization may form CH_4 according to reaction (2), and magnesite can form during the serpentinization process as in reaction (3). Formation of $CH_{4(g)}$ directly from graphite and $H_{2(g)}$ is also possible, according to reaction (4):

$$18Mg_2SiO_4 + 6Fe_2SiO_4 + 26H_2O + CO_2$$
$$\rightarrow 12Mg_3Si_2O_5(OH)_4 + 4Fe_3O_4 + CH_4 \tag{2}$$
$$2Mg_2SiO_4 + 2H_2O + HCO_3^-$$
$$\rightarrow MgCO_3 + Mg_3Si_2O_5(OH)_4 + OH^- \tag{3}$$
$$C + 2H_2(g) \rightarrow CH_4(g). \tag{4}$$

The presence of goethite and hematite indicates an oxidized alteration environment that most probably has a continental influence (Gervilla and Leblanc, 1990). The oxidizing fluids probably altered the peridotite as a separate event from the precipitation of the flaky graphite. The presence of primary Fe–Ni–Cu sulphide assemblages in the rocks (Luque *et al.*, 1992) is an indicator of a reducing environment (Frost, 1985), which prevailed during the formation of the flaky graphite. Pentlandite is a mineral sensitive to high oxygen fugacity (Frost & Beard, 2007), and the presence of pentlandite in the 'Los Pobres' mine suggests a reducing environment at the time of its formation. Our results indicate that 'Los Pobres' graphite mineralizations may have been derived partly from the mantle and partly from the metamorphic activity and concomitant serpentinization at high T, with two major sources of C: mantle-derived and organic C from a continental or sub-continental plate. The organic C is subjected to carbonization at $T < 550$ °C and will produce amorphous, or early amorphous C (Kueter *et al.*, 2019), which is seen in the graphite precipitated in the matrix and veins.

Carbon isotopes are powerful tools to unravel the origin of C in graphitic rocks, and typical mantle values are approximately –5‰, which is commonly found in mid-ocean ridge basalts and peridotitic diamonds (Crespo *et al.*, 2006). Deviations from this value are considered to be due to the mixing of different C sources, which is also the case here, although our study suggests a metamorphic rather than a magmatic origin of parts of the graphite mineralization. With *in situ* C isotope analyses instead of the commonly used bulk analyses, the higher resolution allows for a more precise interpretation of the different graphite precipitation sources, which in some cases may change the overall geological picture.

All rock types, sedimentary as well as felsic, mafic and ultramafic igneous rocks, can contain graphite.

The graphite mineralization in 'Los Pobres' described in this paper is vein-deposited graphite associated with metamorphic precipitation of graphite from melts and/or fluids. The mixed carbon isotopic signature of 'Los Pobres' graphite may indicate an early stage of mantle C assimilation, resulting in preserved signatures from both the mantle and biogenic C sources. The graphite mineralization of Ronda is a rare deposit and can be found in only a few other places in the world, such as in Beni Bousera (Morocco) and Borrowdale (UK). This fact and the relatively minor volume of the 'Los Pobres' mineralization make it less interesting for mining.

CONCLUDING REMARKS

This study suggests that the formation of the 'Los Pobres' graphite occurred in a broad cooling range with graphite deposition in different temperature regimes. Precipitation at high T ($>640\,°C$) resulted in well-defined, pure flaky graphite crystals. At lower T (between 545 and $626\,°C$), C precipitated as poorly crystalline graphite with impurities of trace elements caused by metamorphic alteration of the peridotite during its emplacement. This graphite formation from CO_2- and CH_4-rich fluids resulted in the formation of aqueous fluids. When the cooling temperature reached $500\,°C$ and less, the residual, aqueous fluids altered the surrounding rocks and caused strong serpentinization of the host rock and numerous veins cross-cutting both the graphite and host rocks. The isotopic composition of the graphite mineralization reflects a mixture of different C sources, where organic and mantle-derived C provides the observed mixed isotopic signature.

SUPPLEMENTARY DATA

Supplementary data are available at *Journal of Petrology online*.

REFERENCES

Beyssac, O., Goffé, B., Chopin, C. & Rouzaud, J. N. (2002a). Raman spectra of carbonaceous material in metasediments: a new geothermometer. *Journal of Metamorphic Geology* **20**, 859–871.

Beyssac, O., Rouzaud, J. N., Goffé, B., Brunet, F. & Chopin, C. (2002b). Graphitization in a high-pressure, low-temperature metamorphic gradient: a Raman microspectroscopy and HRTEM study. *Contributions to Mineralogy and Petrology* **143**, 19–31.

Beyssac, O., Goffé, B., Petitet, J.-P., Froigneux, E., Moreau, M. & Rouzaud, J.-N. (2003). On the characterization of disordered and heterogeneous carbonaceous materials by Raman spectroscopy. *Spectrochimica Acta Part A: Molecular and Biomolecular Spectroscopy* **59**, 2267–2276.

Compagnini, G., Puglisi, O. & Foti, G. (1997). Raman spectra of virgin and damaged graphite edge planes. *Carbon* **35**, 1793–1797.

Crespo, E., Luque, F. J., Rodas, M., Wada, H. & Gervilla, F. (2006). Graphite–sulfide deposits in Ronda and Beni Bousera peridotites (Spain and Morocco) and the origin of carbon in mantle-derived rocks. *Gondwana Research* **9**, 279–290.

Dickey, J. S. & Obata, M. (1974). Graphitic hornfels dikes in Ronda high-temperature peridotite massif. *American Mineralogist* **59**, 1183–1189.

Downs, R. T. (2006). The RRUFF Project: an integrated study of the chemistry, crystallography, Raman and infrared spectroscopy of minerals. Program and Abstracts of the 19th General Meeting of the International Mineralogical Association in Kobe, Japan, O03-13.

Esteban, J. J. (2011). Birbirite occurrence in the Ronda peridotites (Betic Cordilleras, southern Spain. *Geophysical Research Abstracts* **13**, EGU2011-1891-2.

Esteban, J. J., Tubía, J. M. & Cuevas, J. (2005). Mantle diapirism in a converging setting: the example of the Carratraca Massif (Ronda Peridotites), Spain. *Ofioliti* **30**, 167–168.

Evans, B. V. (2010). Lizardite versus antigorite serpentinite: magnetite, hydrogen, and life (?). *Geology* **38**, 879–882.

Frezzotti, M. L., Tecce, F. & Casagli, A. (2012). Raman spectroscopy for fluid inclusion analysis. *Journal of Geochemical Exploration* **112**, 1–20.

Frost, B. R. (1985). On the stability of sulfides, oxides, and native metals in serpentinite. *Journal of Petrology* **26**, 31–63.

Frost, B. R. & Beard, J. S. (2007). On silica activity and serpentinization. *Journal of Petrology* **48**, 1351–1368.

Frost, R. L., Jagannadha Reddy, B. & Palmer, S. J. (2008). The structure of mimetite, arsenian pyromorphite and hedyphane—A near-infrared spectroscopic study. *Polyhedron* **27**, 1747–1753.

Galvez, M. E., Beyssac, O., Martinez, I., Benzerara, K., Chaduteau, C., Malvoisin, B. & Malavieille, J. (2013). Graphite formation by carbonate reduction during subduction. *Nature Geoscience* **6**, 473–477.

Garrido, C. J. & Bodinier, J.-L. (1999). Diversity of mafic rocks in the Ronda peridotite: evidence for pervasive melt–rock reaction during heating of subcontinental lithosphere by upwelling asthenosphere. *Journal of Petrology* **40**, 729–754.

Garrido, C. J., Gueydan, F., Booth-Rea, G., Precigout, J., Hidas, K., Padrón-Navarta, J. A. & Marchesi, C. (2011). Garnet lherzolite and garnet–spinel mylonite in the Ronda peridotite: Vestiges of Oligocene backarc mantle lithospheric extension in the western Mediterranean. *Geology* **39**, 927–930.

Gervilla, F. & Leblanc, M. (1990). Magmatic ores in high-temperature alpine-type lherzolite massifs (Ronda, Spain, and Beni Bousera, Morocco). *Economic Geology* **85**, 112–132.

Gervilla, F., Leblanc, M., Torres-Ruiz, J. & Fenoll Hach-Alí, P. (1996). Immiscibility between arsenide and sulfide melts: a mechanism for the concentration of noble metals. *Canadian Mineralogist* **34**, 485–502.

Gervilla, F., Gutiérrez-Narbona, R. & Fenoll-Hach-Alí, P. (2002). The origin of different types of magmatic mineralizations from small-volume melts in the lherzolite massifs of the

Serranía de Ronda. *Boletín de la Sociedad Española de Mineralogía* **25**, 79–96.

González-Jiménez, J. M., Marchesi, C., Griffin, W. L., Gervilla, F., Belousova, E. A., Garrido, C. J., Romero, R., Talavera, C., Leisen, M., O'Reilly, S. Y., Barra, F. Y. & Martin, L. (2017). Zircon recycling and crystallization during formation of chromite- and Ni-arsenide ores in the subcontinental lithospheric mantle (Serranía de Ronda, Spain). *Ore Geology Reviews* **90**, 193–209.

Gutierrez-Narbona, R., Lorand, J.-P., Gervilla, F. & Gros, M. (2003). New data on base metal mineralogy and platinum-group minerals in the Ojen chromitites (Serrania de Ronda, Betic Cordillera, southern Spain). *Neues Jahrbuch für Mineralogie, Abhandlungen* **179**, 143–173.

Huang, E.-P., Huang, E., Yu, S.-C., Chen, Y.-H., Lee, J.-S. & Fang, J.-N. (2010). *In situ* Raman spectroscopy on kerogen at high temperatures and high pressures. *Physics and Chemistry of Minerals* **37**, 593–600.

Huizenga, J.-M. (2010). Thermodynamic modelling of a cooling C–O–H fluid–graphite system: implications for hydrothermal graphite precipitation. *Mineralium Deposita* **46**, 23–33.

Ivarsson, M. (2006). Advantages of doubly polished thin sections for the study of microfossils in volcanic rock. *Geochemical Transactions* **7**, 5.

Katagiri, G., Ishida, H. & Ishitani, A. (1988). Raman spectra of graphite edge planes. *Carbon* **26**, 565–571.

Klein, F. & McCollom, T. M. (2013). From serpentinization to carbonation: new insights from a CO_2 injection experiment. *Earth and Planetary Science Letters* **379**, 137–145.

Kouketsu, Y., Mizukami, T., Mori, H., Endo, S., Aoya, M., Hara, H., Nakamura, D. & Wallis, S. (2014). A new approach to develop the Raman carbonaceous material geothermometer for low-grade metamorphism using peak width. *Island Arc* **23**, 33–50.

Kueter, N., Schmidt, M. W., Lilley, M. D. & Bernasconi, S. M. (2019). Experimental determination of equilibrium CH_4–CO_2–CO carbon isotope fractionation factors (300–1200 °C). *Earth and Planetary Science Letters* **506**, 64–75.

Lafay, R., Montes-Hernandez, G., Janots, E., Chiriac, R., Findling, N. & Toche, F. (2014). Simultaneous precipitation of magnesite and lizardite from hydrothermal alteration of olivine under high-carbonate alkalinity. *Chemical Geology* **368**, 63–75.

Lenaz, D. & Lughi, V. (2013). Raman study of $MgCr_2O_4$–$Fe^{2+}Cr_2O_4$ and $MgCr_2O_4$–$MgFe_2^{3+}O_4$ synthetic series: the effects of Fe^{2+} and Fe^{3+} on Raman shifts. *Physics and Chemistry of Minerals* **40**, 491–498.

Lenoir, X. (2001). The recrystallization front of the Ronda Peridotite: evidence for melting and thermal erosion of subcontinental lithospheric mantle beneath the Alboran Basin. *Journal of Petrology* **42**, 141–158.

Luque, F. J. & Rodas, M. (1999). Constraints on graphite crystallinity in some Spanish fluid-deposited occurrences from different geologic settings. Mineralium Deposita **34**, 215–219.

Luque, F. J., Rodas, M. & Galán, E. (1992). Graphite vein mineralization in the ultramafic rocks of southern Spain: mineralogy and genetic relationships. *Mineralium Deposita* **27**, 226–233.

Luque, F. J., Pasteris, J. D., Wopenka, B., Rodas, M. & Barrenechea, T. F. (1998). Natural fluid-deposited graphite: mineralogical characteristics and mechanisms of formation. *American Journal of Science* **298**, 471–498.

Luque, F. J., Crespo-Feo, E., Barrenechea, J. F. & Ortega, L. (2012). Carbon isotopes of graphite: Implications on fluid history. *Geoscience Frontiers* **3**, 197–207.

Majumdar, A. S., Hövelmann, J., Vollmer, C., Berndt, J., Mondal, S. K. & Putnis, A. (2016). Formation of Mg-rich olivine pseudomorphs in serpentinized dunite from the Mesoarchean Nuasahi Massif, Eastern India: insights into the evolution of fluid composition at the mineral–fluid interface. *Journal of Petrology* **57**, 3–26.

Nasdala, L., Smith, D., Kaindl, R. & Ziemann, M. (2004). Raman spectroscopy: analytical perspectives in mineralogical research. *Spectroscopic Methods in Mineralogy* **6**, 281–343.

Negro, F., Beyssac, O., Goffé, B., Saddiqi, O. & Bouybaouène, M. L. (2006). Thermal structure of the Alboran Domain in the Rif (northern Morocco) and the Western Betics (southern Spain). Constraints from Raman spectroscopy of carbonaceous material. *Journal of Metamorphic Geology* **24**, 309–327.

Pimenta, M. A., Dresselhaus, G., Dresselhaus, M. S., Cançado, L. G., Jorio, A. & Saito, R. (2007). Studying disorder in graphite-based systems by Raman spectroscopy. *Physical Chemistry Chemical Physics* **9**, 1276–1290.

Reisberg, L. & Lorand, J. P. (1995). Longevity of sub-continental mantle lithosphere from osmium isotope systematics in orogenic peridotite massifs. *Nature* **376**, 159–162.

Rodas, M., Luque, F. J., Barrenechea, J. F., Fernández-Caliani, J. C., Miras, A. & Fernández-Rodríguez, C. (2000). Graphite occurrences in the low-pressure/high-temperature metamorphic belt of the Sierra de Aracena (southern Iberian Massif). *Mineralogical Magazine* **64**, 801–814.

van der Wal, D. & Bodinier, J. L. (1996). Origin of the recrystallisation front in the Ronda peridotite by km-scale pervasive porous melt flow. *Contributions to Mineralogy and Petrology* **122**, 387–405.

van der Wal, D. & Vissers, R. (1996). Structural petrology of the Ronda Peridotite, SW Spain: deformation history. *Journal of Petrology* **37**, 23–43.

Vauchez, A. & Garrido, C. J. (2001). Seismic properties of an asthenospherized lithospheric mantle: constraints from lattice preferred orientations in peridotite from the Ronda massif. *Earth and Planetary Science Letters* **192**, 235–249.

Wang, A., Dhamenincourt, P., Dubessy, J., Guerard, D., Landais, P. & Lelaurain, M. (1989). Characterization of graphite alteration in an uranium deposit by micro-Raman spectroscopy, X-ray diffraction, transmission electron microscopy and scanning electron microscopy. *Carbon* **27**, 209–218.